JGR Atmospheres

RESEARCH ARTICLE
10.1029/2020JD033921

Simultaneous Observations of EIP, TGF, Elve, and Optical Lightning

N. Østgaard[1], S. A. Cummer[2], A. Mezentsev[1], A. Luque[3], J. Dwyer[4], T. Neubert[5], V. Reglero[6], M. Marisaldi[1,7], P. Kochkin[1], D. Sarria[1], N. Lehtinen[1], K. Ullaland[1], S. Yang[1], G. Genov[1], O. Chanrion[5], F. Christiansen[5], and Y. Pu[2]

[1]Department of Physics and Technology, Birkeland Centre for Space Science, University of Bergen, Bergen, Norway, [2]Electrical and Computer Engineering, Duke University, Durham, NC, USA, [3]Instituto de Astrofísica de Andalucía, Glorieta de la Astronomia, Grenada, Spain, [4]Department of Physics, University of New Hampshire, Durham, NH, USA, [5]National Space Institute, Technical University of Denmark, Kgs. Lyngby, Denmark, [6]Image Processing Laboratory, University of Valencia, Paterna, Valencia, Spain, [7]INAF-OAS Bologna, Bologna, Italy

Abstract On February 8, 2019, the Atmosphere-Space Interaction Monitor observed a terrestrial gamma-ray flash (TGF) and an Elve from a positive intracloud (+IC) lightning during the initial breakdown stage of a lightning flash north east of Puerto Rico. A second Elve produced by the return stroke (RS) of a negative cloud-to-ground (−CG) lightning was observed 456 ms later about 300 km south of the first one. Radio measurements show that a short (30 μs) and large (280 kA km) energetic in-cloud pulse (EIP) produced the electromagnetic (EM) wave for the first Elve while the RS of the −CG was the EM source for the second Elve. Assuming that the EIP and the RS were the sources of the 777 nm emissions, both the delay relative to the ultra-violet pulse and the shape and duration of the 777 nm emissions can be explained by scattering and absorption inside the clouds. The TGF produced by the +IC lightning had the same duration as the EIP (~30 μs). Due to the ±80 μs timing uncertainty of the TGF, we can only state that TGF was produced just before or most likely simultaneously with the EIP. The large 777 nm pulse indicates that a large part of the EIP was produced by a current flowing in a hot channel, but it is likely that the TGF current also contributed significantly to the EIP.

Key Points:

- An Elve and a TGF were produced during the vertical leader propagation in the initial phase of a positive intracloud lightning
- A short and strong current observed as an energetic in-cloud pulse (EIP) produced both the EMP for the Elve and the large optical pulses
- The EIP was likely produced by a combination of a current in a hot leader and the TGF current

Supporting Information:

Supporting Information may be found in the online version of this article.

Correspondence to:

N. Østgaard,
nikolai.ostgaard@uib.no

Citation:

Østgaard, N., Cummer, S. A., Mezentsev, A., Luque, A., Dwyer, J., Neubert, T., et al. (2021). Simultaneous observations of EIP, TGF, Elve, and optical lightning. *Journal of Geophysical Research: Atmospheres*, *126*, e2020JD033921. https://doi.org/10.1029/2020JD033921

Received 21 SEP 2020
Accepted 2 APR 2021

Author Contributions:

Conceptualization: N. Østgaard
Data curation: S. A. Cummer, A. Luque, T. Neubert, P. Kochkin, D. Sarria, K. Ullaland, S. Yang, G. Genov, O. Chanrion, F. Christiansen, Y. Pu
Formal analysis: N. Østgaard, S. A. Cummer, A. Mezentsev, J. Dwyer
Funding acquisition: N. Østgaard, T. Neubert, V. Reglero
Investigation: N. Østgaard, A. Mezentsev
Methodology: N. Østgaard, A. Mezentsev
Project Administration: N. Østgaard

1. Introduction

Terrestrial gamma-ray flashes (TGFs) are short flashes of high energy photons up to ~40 MeV observed by many platforms over the last 3 decades (Bogomolov et al., 2017; Briggs et al., 2010; Fishman et al., 1994; Marisaldi et al., 2010; Smith et al., 2005; Ursi et al., 2017). It was early established that they originate from thunderstorms, but how they are connected to the various processes in lightning is still an open question. Spectral analysis (Dwyer & Smith, 2005) and radio measurements (Cummer et al., 2015) have shown that TGFs observed from space are produced inside thunderclouds (10–15 km altitude) in association with positive intracloud (+IC) lightning (Cummer et al., 2005; Stanley et al., 2006). Several studies have shown that TGFs are typically produced in the *initial* phase of lightning flashes during the upward propagation of leaders (Cummer et al., 2011; Lu et al., 2010; Østgaard et al., 2013; Shao et al., 2010). Recently, it has been reported that TGFs are frequently observed simultaneously with energetic in-cloud pulses (EIPs) (Cummer et al., 2014; Pu et al., 2019). Theoretical considerations (Cummer et al., 2014; Lyu et al., 2015) and modeling (Liu et al., 2017) have suggested that the EIPs related to TGFs should also produce Elves, which can be observed as rings of ultra-violet (UV) emissions produced by an electromagnetic pulse (EMP) from a short and strong current pulse, when the EMP hits the ionosphere from below and excites N_2 molecules. Earlier modeling efforts have related Elves doublets to compact intracloud discharges, which have similar characteristics as EIPs (duration and intensity), but are assumed to be produced at higher altitudes (Marshall et al., 2015). This prediction of an Elve and a TGF produced by the same discharge was confirmed by the first results from Atmosphere-Space Interaction Monitor (ASIM) by Neubert et al. (2020), where both optical and gamma-ray imaging and light curves showed that an Elve and a TGF were produced by the same lightning within 20 ± 5 μs. The first effort to relate both radio measurements and optical signals from lightning and TGFs and to understand the sequence of events was reported by Østgaard et al. (2013). Unfortunately, as later pointed out by Gjesteland et al. (2017), the time resolution of the optical measurements was not sufficient to make any unambiguous conclusions. With the launch of ASIM in 2018, this question

Resources: N. Østgaard, T. Neubert, V. Reglero, K. Ullaland, S. Yang, G. Genov, O. Chanrion, F. Christiansen
Software: N. Østgaard, S. A. Cummer, A. Mezentsev, A. Luque, J. Dwyer, Y. Pu
Supervision: N. Østgaard
Validation: N. Østgaard, S. A. Cummer, A. Mezentsev, A. Luque, J. Dwyer, M. Marisaldi, D. Sarria, N. Lehtinen, Y. Pu
Writing – original draft: N. Østgaard
Writing – review & editing: M. Marisaldi, P. Kochkin, D. Sarria, N. Lehtinen, Y. Pu

could be revisited, and Østgaard, Neubert, et al. (2019) reported that the majority of the observed TGFs that also had associated optical measurements (nighttime observations) were produced simultaneously (±80 μs) with a large optical pulse from IC lightning, but a significant part of the TGFs was produced before the onset of the large optical pulse. The effects of scattering and absorption of light during its propagation through the cloud were not accounted for in that study, and the large optical pulse was interpreted to be produced by a large current pulse flowing in the hot channel of an upward propagating leader.

In this study, we present a unique combination of data obtained when an +IC lightning produced both an Elve and a TGF, and 456 ms later a negative cloud-to-ground (−CG) lightning, 300 km south of the +IC lightning, produced a second Elve. With high-resolution gamma-ray measurements of the TGF, high-resolution optical measurements in two optical bands of the lightning, UV measurements of the two Elves and low-frequency (LF) radio measurements from both lightning, we have explored in detail the time sequence of events around the TGF generation. The locations of the two parent lightning were given by World Wide Lightning Location Network (WWLLN) and GLD360 (Vaisala) and were consistent with the camera images of the lightning. We also show that modeling of the Elve from the observed EIP as well as scattering and absorption effects of the light propagation through the cloud is important for interpreting the time sequence of events.

2. Instruments and Data

The ASIM payload (Neubert et al., 2019) consists of two main instruments, the modular X- and gamma-ray sensor (MXGS) (Østgaard, Balling, et al., 2019) and the modular multispectral imaging array (MMIA) (Chanrion et al., 2019). ASIM is mounted on the International Space Station (ISS) orbiting the Earth at about 400 km altitude with an inclination of 51.6°. The MXGS consists of two detectors for detecting X- and gamma-rays. The MXGS low-energy detector (LED) is a pixelated layer of cadmium-zinc-telluride detector crystals sensitive to photons with energies from 50 to 400 keV. The effective detection area at 100 keV is ∼400 cm^2. Temporal resolution of the LED is about 1 μs with a dead-time of about 1.4 μs. The MXGS high energy detector (HED) comprises 12 bismuth-germanium-oxide (BGO) detector bars with each coupled to a photomultiplier tube (PMT). The geometric detector area of HED is 900 cm^2 and is sensitive to photons with energies from 300 keV to >30 MeV. The effective detection area for HED is ∼650 cm^2 at 1 MeV. The HED is mounted behind the LED. Temporal resolution of the HED is 28.7 ns with a dead-time of about 550 ns for detection by the same PMT/BGO detector module. The MXGS characteristics are summarized in Table 1. The MMIA has two cameras imaging 337.0 nm (CHU1) and 777.4 nm (CHU2) emissions, at up to 12 frames per second (83 ms exposure), and three high-speed photometers (PHOT 1–3) at 337.0 nm (bandwidth 5 nm), 180–230 nm, and 777.4 nm (bandwidth 4 nm) with a 100 kHz sampling rate. The 777.4 nm emissions are from atomic oxygen and used for detecting lightning. Emissions in the Lyman–Birge–Hopfield (LBH) UV band (180–230 nm) are affected by molecular absorption of ozone and molecular oxygen and therefore this band is most sensitive to high-altitude phenomena. The 337.0 nm ($N_2$2P) band will be most sensitive to lightning, but as it is close to the UV band, it will also see weak signals similar to the UV emissions (Chanrion et al., 2019). The field of view (FOV) of the cameras and the two photometers are square with 80° diagonal, while the UV photometer FOV is circular with 80° full cone angle. The MMIA characteristics are summarized in Table 2. The two instruments, MMIA and MXGS, constitute a cross-triggered system. This means that when a TGF is detected the MMIA gets a trigger signal and captures 2 s of data. When MMIA sees an optical signal above a certain level, MXGS receives a trigger and captures 2 s of data. The relative timing between MXGS and MMIA was ±80 μs for the February 8, 2019, event. After an upgrade of the onboard software implemented in March 2019, the relative timing accuracy is ±5 μs for all triggered events. The absolute time tagging of the ASIM instruments is varying stochastically between 0 and 20 ms. However, due to the two Elve signatures in the UV band, the LF data, and the WWLLN and GLD360 data, we were able to align the LF and UV data with a 10 μs accuracy (see Sections 3.2 and 3.3).

Table 1
Characteristics of MXGS

Detector	Energy range	Effective area	Temporal resolution
LED	50–400 keV	400 cm^2 (at 100 keV)	1 μs
HED	300 keV to >30 MeV	650 cm^2 (at 1 MeV)	28.7 ns

The LF radio emissions (30–300 kHz) were recorded in Puerto Rico at 18.3468°N latitude and −66.7520°E longitude. The sensor has a flat frequency response from 100 to 200 kHz and a frequency-proportional re-

Table 2
Characteristics of MMIA

Instrument	Band/width (nm)	FOV	Temporal resolution
PHOT 1	337.0/4	Square 80° diagonal	10 μs
PHOT 2	180–230	Circular 80° diagonal	10 μs
PHOT 3	777.4/5	Square 80° diagonal	10 μs
CHU 1	337.0/4	Square 80° diagonal	>83 ms
CHU 2	777.4/5	Square 80° diagonal	>83 ms

sponse from 1 to 100 kHz. Absolute amplitude calibration was obtained from both laboratory measurements and in-field cross calibration with other magnetic sensors. GPS timing ensures absolute timing accuracy of several microseconds. The LF radio measurements are used to derive current moments on a time scale of 5 μs to 1 ms.

The WWLLN with more than 70 very low frequency (VLF) sensors around the globe provides lightning geolocation and timing (see http://wwlln.net). The time of group arrival technique provides average accuracy of 5 km and 10 μs, which varies significantly with geographical origin of the storm (Hutchins et al., 2012; Rodger et al., 2005). To geolocate a lightning event, WWLLN needs to detect the VLF sferics by at least five stations (Rodger et al., 2005).

GLD360 is another network of ground-based lightning sensors (500 Hz to 50 kHz) detecting both CG and IC lightning with a median location accuracy of 2.5 km. The GLD360 sensors use a combination of magnetic direction finding and time-of-arrival techniques (from at least four stations) to geolocate the lightning source (Rudlosky et al., 2017; Said et al., 2010).

The GOES-16 satellite (band 16) provides 15 min scan in 13.3 μm wavelength (CO_2 longwave infrared band) of cloud coverage with a 2 km spatial resolution (Schmit et al., 2016).

3. Observations

3.1. Overview

Figure 1 shows the position (red dot) of the ISS on February 8, 2019, at 00.01:38 UT north-east of Puerto Rico during the two Elve detections. The green dots are the lightning activity detected by WWLLN within ±1,000 s around the TGF. The geolocations from WWLLN for the two Elve producing lightning are shown by magenta dots. The first Elve was produced by a lightning about 100 km west of ISS (one magenta dot) while the second Elve was produced from a lightning in a separate cloud 300 km south of the first one (two magenta dots). Radio signals from both lightning were detected by the LF receiver in Puerto Rico (white star) ~1,250 km and ~1,220 km away. The cloud coverage measured by GOES-16 spacecraft is also shown. This is a 15 min scan with 13.3 μm wavelength giving a 2 km resolution. The clouds close to ISS were scanned approximately 5 min into the scan (~00:05:00 UT).

Figure 2 gives an overview of our measurements. The two spikes in Figure 2b are the UV signals from the Elves, which are separated 456 ms in time, the same separation reported by WWLLN (blue vertical lines), GLD360 (green vertical lines), and LF radio from Puerto Rico (Figure 2d) of an EIP in a +IC discharge and a return stroke (RS) in a −CG discharge. Due to this alignment in time, our absolute timing is not the nominal 0–20 ms accuracy of ASIM but is given by the lightning networks and the LF data, and the MMIA photometer data are aligned such that the first UV peak coincides with the WWLLN, GLD360, and LF data. In Sections 3.2, 3.3, and 4.2, we describe in more detail how the LF and UV data are aligned with a ~10 μs accuracy. Figures 2e and 2f show the MMIA camera images in 337 and 777 nm wavelength (logarithmical scale). Red circles indicate the locations of the Elve producing lightning, which coincide with the geolocation obtained by WWLLN and GLD360. The lightning that produced the first Elve also produced a TGF and was the first large optical pulse in a lightning flash that lasted for about 500 ms (Figures 2a, 2c, 2e, and 2f). From only the light curves of the optical signals, it may look like the lightning that produced the second Elve belonged to the same flash. However, this is not the case, as it came from lightning in a different cloud 300 km south of the first one. As no activity is seen from this location in the previous camera images or by WWLLN or GLD360, it was the first large optical pulse from that location.

3.2. TGF, Elve, and Optics From the +IC Discharge

Figure 3 shows three milliseconds of data around the TGF and the first Elve. To find the location and time of the source, we have used both WWLLN and GLD360 detections of the source combined with the LF data

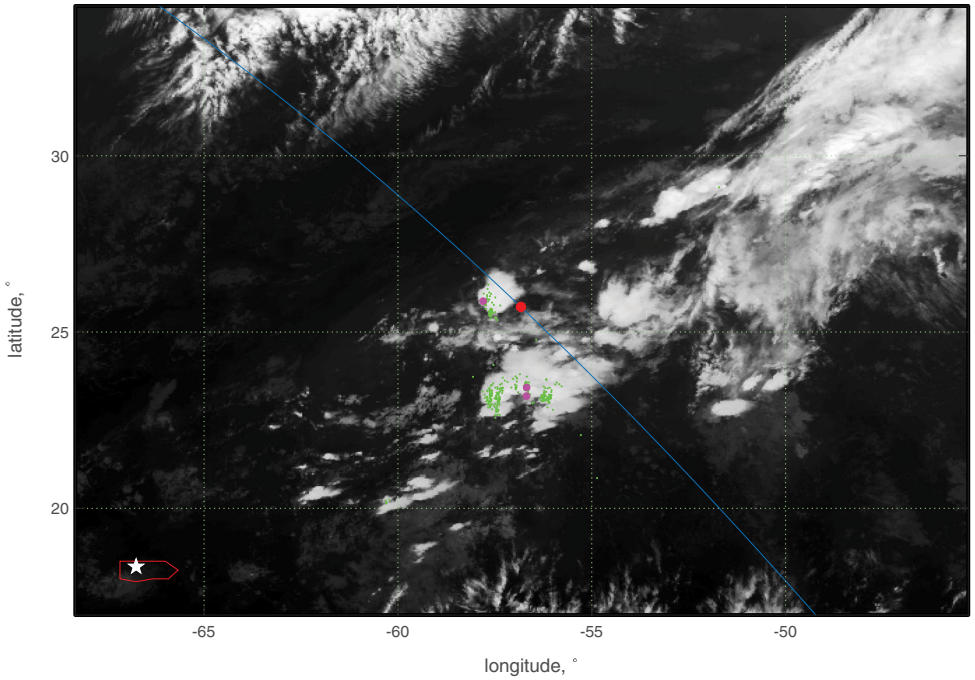

Figure 1. A map of the event measured by ASIM on February 8, 2019, at 00.01:38 UT. Red dot is the location of the International Space Station (ISS) during the two Elve detections and blue line shows its trajectory. Green dots are the WWLLN activity ±1,000 s of the TGF. Magenta dots are the WWLLN detections associated with the two Elves. White star is the location of the LF receiver in Puerto Rico (marked with red). Cloud coverage is from GOES-16, band 16 by a 15 min scan starting at 00.00:00 UT. ASIM, Atmosphere-Space Interaction Monitor; WWLLN, World Wide Lightning Location Network; TGF, terrestrial gamma-ray flash; LF, low frequency.

and proceeded as follows: The two locations and times (47 μs apart), detected respectively by WWLLN and GLD360, were used to forward propagate the times to the Puerto Rico LF receiver. It was found that the average between the two locations and times gives the most precise arrival time at the Puerto Rico station within a few μs of the onset of the pulse in the LF data. We therefore used this average location, which is within the uncertainties of both WWLLN and GLD360 location, for propagating the LF data back to source. GLD360 reported a peak current of +257 kA. The MMIA photometer data were aligned such that the onset of the UV pulse coincides with the onset of the LF pulse, with a 10 μs delay, which will be explained in Section 4.2. This means that the only assumption we have made for time aligning the MMIA and LF data is that the large LF pulse of the EIP (see Section 4.1) is the source of the UV pulse of the Elve. Finally, the MXGS data have a relative timing uncertainty of ±80 μs relative to MMIA and are shown by the horizontal black line in Figure 3b.

Figure 3a shows the bipolar nature of the large LF pulse and the discrete (as opposed to continuous) pulse activity before and after the signal. This, along with the polarity of the leading edge of the pulse, indicates that this signal was produced by an IC lightning pulse with positive field polarity, and thus from an upward propagating negative leader (Lyu et al., 2015). In the 1-ms interval before the large optical pulses, there are three weak radio pulses (marked with green vertical lines) and gradually increasing weak optical signals in 337 and 777 nm (Figures 3c and 3e). This can also be seen in Figure A1 in Section A1, where 3-ms of LF radio, 337, and 777 nm data are shown in logarithmic scale. Similar preactivity in the optical measurements termed "leader propagation" was reported by Østgaard, Neubert, et al. (2019) and Neubert et al. (2020), and here the LF radio measurements show the discrete pulsed nature of the radio emissions, consistent with upward leader stepping. The Elve is seen in Figure 3d (UV pulse) with a fast rise time of ~100 μs and a duration of ~800 μs. The onset of the optical signal from the lightning seen in 777 nm (Figure 3e) is delayed by ~70 μs compared to the onset of the UV pulse. The 777 nm has a rise time of ~200 μs and duration of ~2 ms. The 337 nm signal has the same duration and shape as the 777 nm but has its onset simultaneous with the UV signal, because 337 nm is also sensitive to the signal from the Elve. The fast rise time, the high

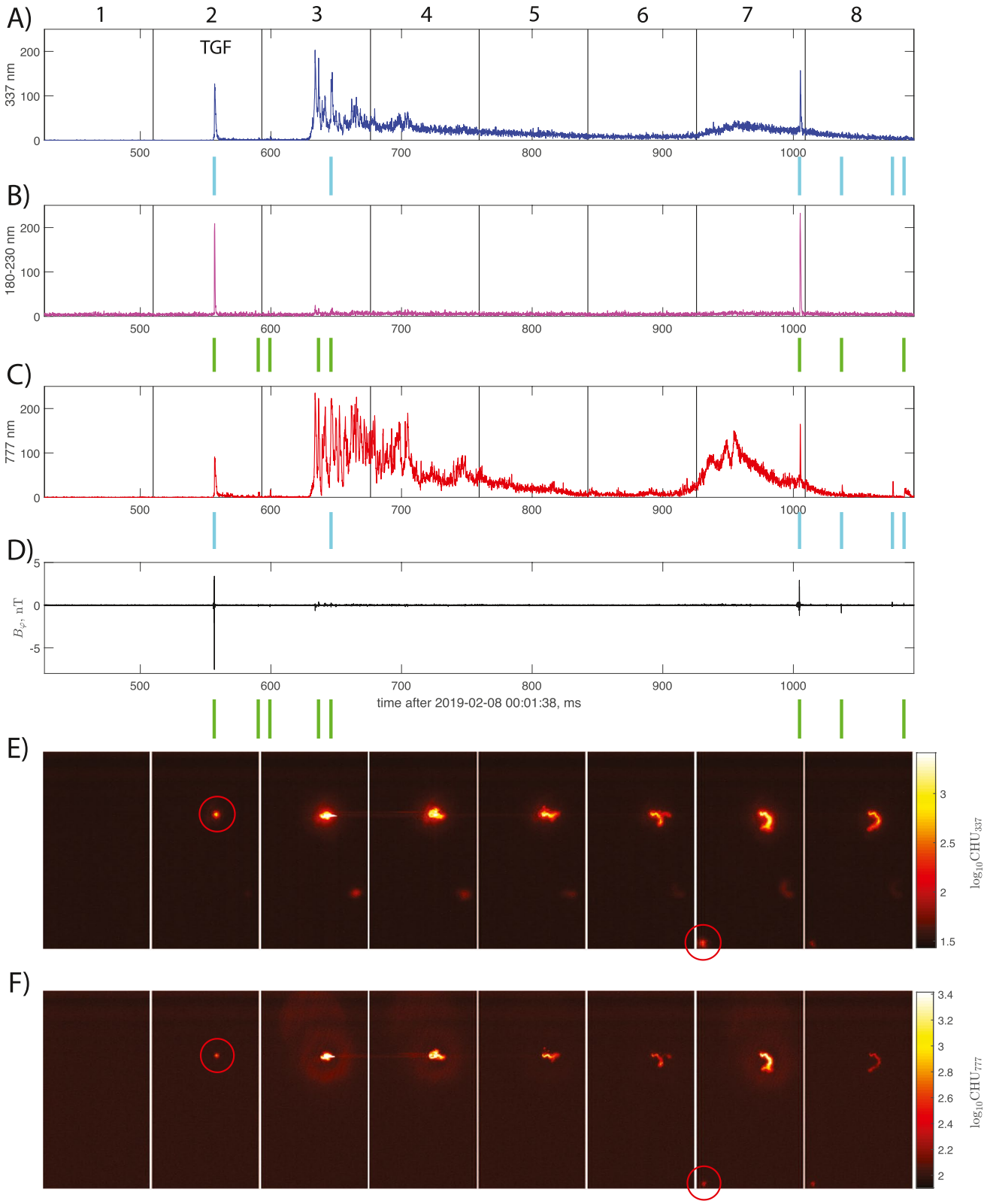
A)
1
2
3
4
5
6
7
8
TGF
337 nm
B)
180-230 nm
C)
777 nm
D)
B_φ, nT
time after 2019-02-08 00:01:38, ms
E)
$\log_{10}$CHU$_{337}$
F)
$\log_{10}$CHU$_{777}$

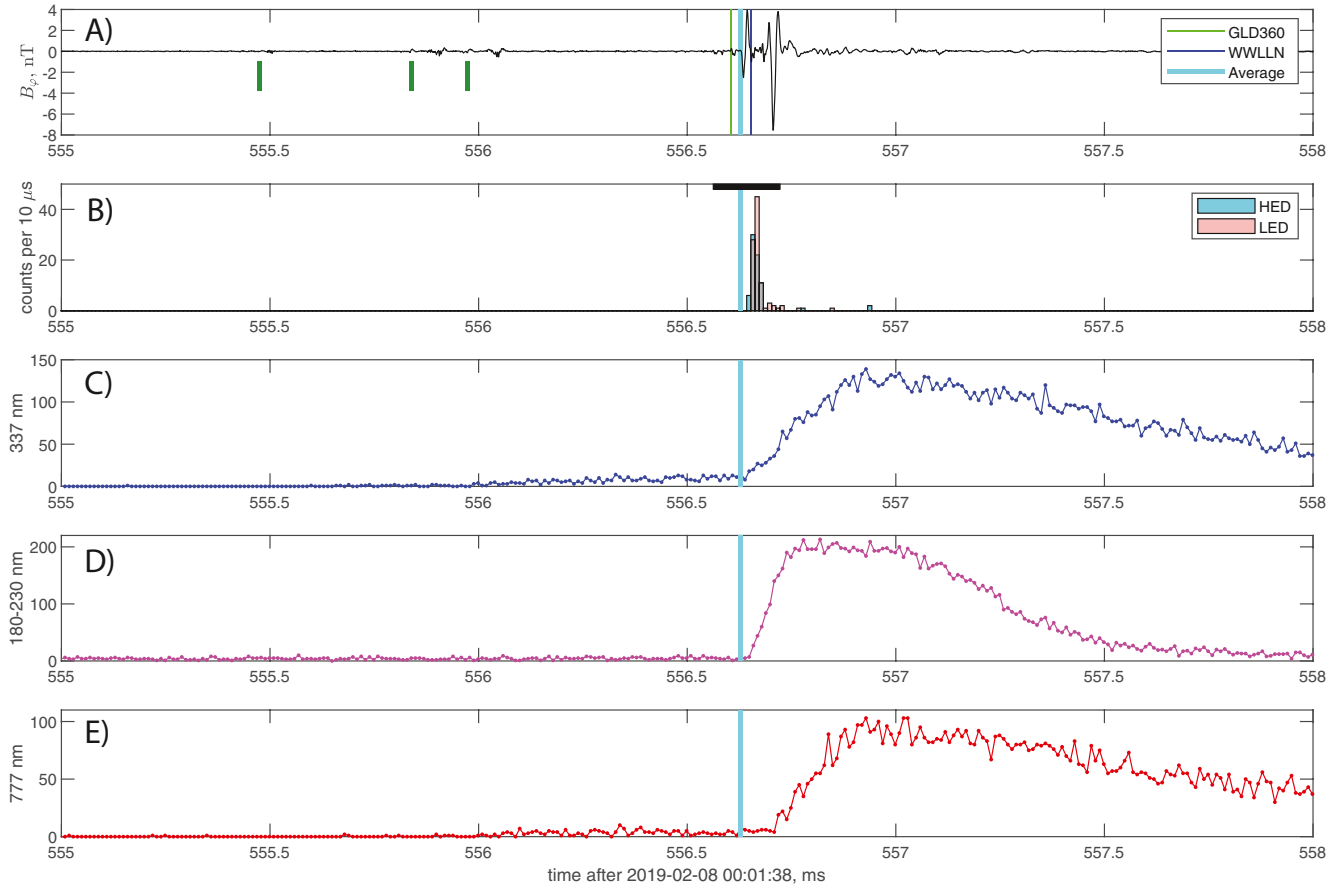

Figure 3. Measurements of the simultaneous EIP, TGF, and Elve in milliseconds after 00.01:38 UT at the source. (a) LF from Puerto Rico with GLD360 and WWLLN. The source time of the average location is marked with thick light blue in all panels (see text for explanation). The vertical green lines indicate leader steps (see text for interpretation). (b) MXGS LED and HED measurements. Black horizontal line shows the ±80 μs relative uncertainty between MXGS and MMIA. (c) MMIA PHOT 337 nm. (d) MMIA PHOT UV 180–230 nm (LBH), (e) MMIA PHOT 777 nm. For panels (c)–(e), the intensities are in ADC units. EIP, energetic in-cloud pulse; TGF, terrestrial gamma-ray flash; LF, low frequency; WWLLN, World Wide Lightning Location Network; MXGS, modular X- and gamma-ray sensor; LED, low-energy detector; HED, high energy detector; MMIA, modular multispectral imaging array; LBH, Lyman–Birge–Hopfield.

intensity of the UV signal, and that it precedes the 777 nm emissions indicate clearly that this is an Elve. As will be shown in Section 4.3, the delay in the 777 nm emissions can be explained by cloud scattering, while the EM pulse that produces the Elve is not delayed by scattering. We often see UV signals from the lightning itself, but those are much weaker and follow the shape of the light curves of the other optical channels. The TGF is on the same time line as the MMIA data with the relative ±80 μs uncertainty shown by the black horizontal bar in Figure 3b. The TGF duration in the HED was only 30–40 μs with photon energies ranging from 50 keV (LED) up to several tens of MeV (HED). The count rate was so high in HED that the instrument was missing counts during the peak intensity.

Figure 2. An overview of measurements. (a) MMIA PHOT 337 nm, with the time of the TGF marked in the second frame, (b) MMIA PHOT UV 180–230 nm (LBH), (c) MMIA PHOT 777 nm, (d) LF radio from Puerto Roco, (e) MMIA camera 337 nm (log-intensity) with 83 ms exposure, and (f) MMIA camera 777 nm (log-intensity) with 83 ms exposure. Red circles in (e and f) are the location of +IC (frame 2) and −CG (frame 7). Numbers above panel (a) are the frame numbers of the camera, and the black vertical lines show the time intervals of the image frames. The vertical blue and green lines between the panels are the sferics detected by WWLLN and GLD360, respectively. For panels (a–c), the intensities are in ADC units. MMIA, modular multispectral imaging array; TGF, terrestrial gamma-ray flash; LBH, Lyman–Birge–Hopfield; LF, low frequency; IC, intracloud; CG, cloud-to-ground; WWLLN, World Wide Lightning Location Network.

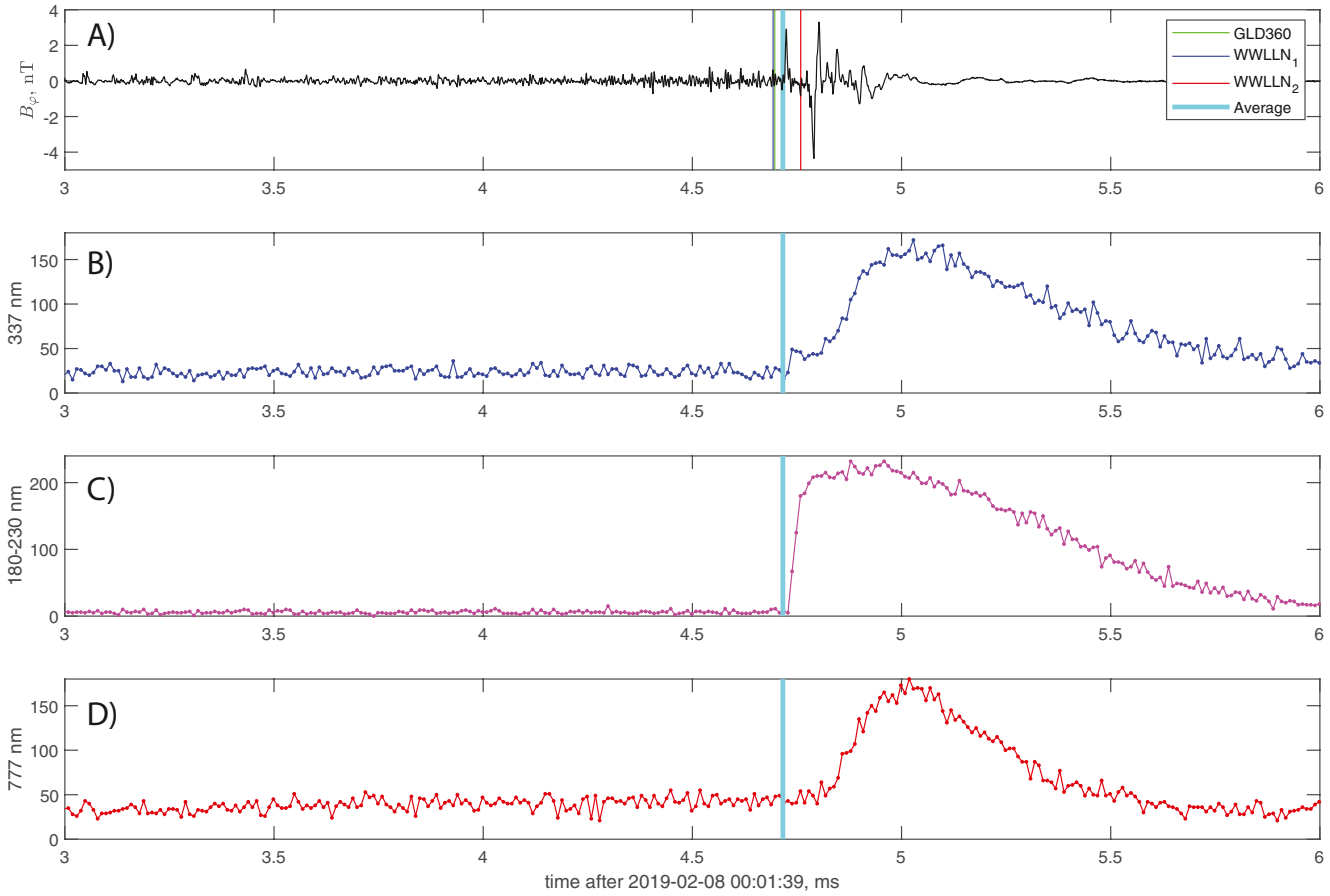

Figure 4. Measurements of the second Elve in milliseconds after 00.01:39 UT at the source. (a) LF from Puerto Rico with two WWLLN location and one GLD360 location. The source time of the average location is shown by a thick light blue line in all panels (see text for explanation). (b) MMIA PHOT 337 nm. (c) MMIA PHOT UV 180–230 nm (LBH). (d) MMIA PHOT 777 nm. For panels (c–e), the intensities are in ADC units. LF, low frequency; WWLLN, World Wide Lightning Location Network; MMIA, modular multispectral imaging array; LBH, Lyman–Birge–Hopfield.

3.3. Elve and Optics From the −CG Discharge

Figure 4 shows three milliseconds of data around the second Elve. In this case, there are two WWLLN locations and one GLD360 location. The same procedure as used for the first Elve was applied to get the location that matched the arrival of the LF pulse, and the LF data were then back-propagated in time using the averaged location. The MMIA data are aligned such that the UV onset is simultaneous with the onset of the LF data, with a 10 μs delay, due to geometry, lifetime of excited states of N_2 molecules, and sensitivity of the photometer (see Section 4.2). Figure 4a shows the continuous LF activity preceding the large pulse for several milliseconds and the monopolar nature of the large pulse. This, along with the polarity of the leading edge of the pulse, indicates that this signal was produced by a −CG lightning discharge (Lyu et al., 2015). The continuous activity for about 2 ms before the large LF pulse is also typical for a downward propagating negative leader of a −CG. As can be seen in Figure A2 in Appendix A, this continuous LF activity (starting at ~2.6 ms, marked with blue bar) before the RS pulse (at ~4.7 ms, marked with red bar) is 1 order of magnitude higher than the level of activity from the previous +IC flash. The intense UV signal from the Elve (Figure 4c) had a faster rise time (~30 μs) and a shorter duration (~600 μs) than seen in the first Elve. The onset of optical pulse in 777 nm (Figure 4d) is delayed relative to the UV pulse by ~90 μs. The optical pulse has a rise time of ~190 μs and a duration of only ~500 μs. Here, we can also clearly see that the 337 nm picks up some signal from the Elve, but otherwise follows the profile of the 777 nm with slightly longer duration. The optical signal in both 337 and 777 nm prior to the large pulse is the superposition of the decaying activity from the +IC flash 300 km north of the −CG as explained in Section 3.1 and the leader propagation before the RS in the −CG stroke.

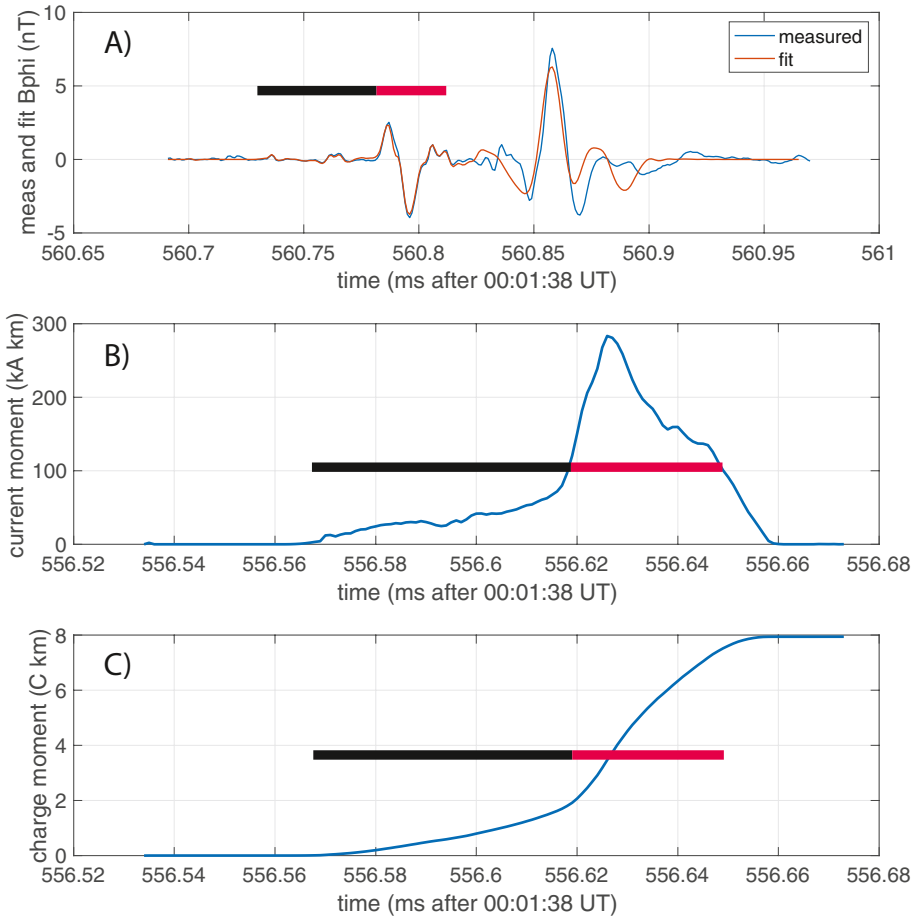

Figure 5. (a) The LF radio signal from the +IC lightning detected at Puerto Rico (blue) overlaid the best fit from a current pulse (red). Time refers to Puerto Rico. (b) The current moment that gives the magnetic signal in the time interval shown by black and red horizontal bars in (a). The EIP is the 30 μs long pulse seen between 556.62 and 556.65 ms marked with red bar. (c) The corresponding charge moment. Both (b and c) have been propagated back in time with the speed of light to the source 1,250 km away (~4 ms). LF, low frequency; IC, intracloud; EIP, energetic in-cloud pulse.

4. Modeling

4.1. Derivation of Current and Charge Moments

We compute the current moment waveform that best fits the measured LF signal using the inversion approach described by Cummer and Inan (2000). In this implementation, we assume a short dipole source and model the propagation impulse response using the well-known time domain field expressions given by Uman et al. (1975), with additional low-pass filtering to account for the ground wave attenuation over sea water (ITU, 2007, https://www.itu.int/rec/R-REC-P.368-9-200702-I/en). We then use deconvolution to find the source waveform consistent with the theoretical impulse response and the measured LF fields (Cummer & Inan, 2000). Linear regularization is employed in this inversion for well posedness and also to ensure that we find the waveform with the minimum total charge moment change that is consistent with the measurement.

Figure 5a shows the reconstructed signal (red) from the source current moment pulse required to produce the measured signal (blue) between 560.70 and 560.95 ms (time interval refers to time at Puerto Rico). In Figure 5b, the best fitted current moment waveform, calibrated in units of kA km at source (~4 ms earlier, 1,250 km away), is shown. A weak current starts about 50 μs before the big pulse, due to the small pulses seen in Figure 5a between 560.73 and 560.78 ms (Puerto Rico time—marked with black horizontal bar) and reaches about 60 kA km before the big pulse between 556.62 and 556.65 ms (source time) seen in Figure 5b.

The big current pulse produces the direct wave signal at 560.78–560.81 ms (Puerto Rico time—marked with red horizontal bar) in Figure 5a. The larger pulse seen from 560.85 ms is the ionospheric reflection. The duration of the main peak of the current moment waveform is ~30 μs and the rise time $\left(\frac{dI}{dt} > 0\right)$ is only 10 μs (see red bar in Figure 5b). This EIP had a peak current moment of 280 kA km and combined with its large $\frac{dI}{dt}$ a big EMP was emitted that produced UV emissions of the Elve. The uncertainty of the current moment values is 10%–20%. For this lightning stroke, GLD360 reported a positive peak current of 257 kA. Figure 5c shows the extracted charge moment, where charge transfer both before and during the EIP reached a total value of 8 C km. About 60% of the charge transfer occurred during the 30 μs long EIP.

4.2. Modeling of the UV Signal From the Elve

To model the expected UV pulse shape for the first Elve seen by the UV photometer, the current moment waveform of the EIP (between 556.618 and 556.660 ms in Figure 5b) was used as a source of the EM pulse. The power converted into the UV light emission is assumed to be proportional to the squared radiative component of the electric field produced by the EIP at the point of UV emission. This, in turn, is proportional to the squared time derivative of the EIP current moment waveform, inverse proportional to the squared distance from source, and modulated by the directional diagram to account for the angular distribution of the power emission. Also, there was implemented an exponential relaxation with 56 μs characteristic time for the excited states of N_2 molecules that emit in the LBH band (Šimek, 2014). Expanding rings of the UV emission at altitude of 90 km were then propagated to the ISS position and integrated over the FOV of the UV photometer to produce the light curve of the modeled UV pulse. To model the second Elve from the −CG RS, the current moment waveform of a Gaussian pulse with $\sigma = 10$ μs and total duration of 30 μs was used as a source of the EM pulse. The geometry for the two sources corresponds to the actual observation geometry (relative position of the two sources and the ISS); the two sources were placed at 13 km (EIP) and 2 km (RS) altitude above the perfectly conductive ground correspondingly.

For the angular modulation of the EMP, we have used Equation 7 from Shao et al. (2004):

$$I(\theta) \sim (1 - \beta\cos\theta)^{-2} \sin^2\theta \tag{1}$$

where θ is the emission angle, $I(\theta)$ is the power emitted to the infinity within the angle cone (θ), and β is the relativistic factor, v/c. In Shao et al. (2004), the speed, v, is the propagation speed of the current wave along the channel. Following Marshall et al. (2015), we set v equal to $0.75c$ but also show the solution for $v = 0.5c$. It is not obvious that one can take an equation which is developed for charged particle motion and use it for a current wave. The wave can move with relativistic velocities, but the current carriers have nonrelativistic speed. To illustrate what the dipole approach is for $v \ll c$, we also show the solution for $\beta = 0$. However, it is beyond the scope of this paper to explore this further. Our purpose for this modeling is to show that the shape of the observed UV signal is what is expected from an Elve and to define the onset of the UV signal as observed by ASIM.

Figure 6 shows the modeling results compared with the observed UV light curves. Figures 6a and 6c show 3,100 and 120 μs of the first Elve and Figures 6b and 6d show 3,100 and 120 μs of the second Elve (all curves are normalized by the maximum value). For both Elves, it can be seen that the UV onset of the observed light curves is delayed by about 10 μs compared to the onset of the modeled UV light curves. This is a combined effect of the instrument's sensitivity (dynamic range ~2 orders of magnitude), the noise level of the UV signal, observational geometry, lifetime of the UV emissions, and the steepness of the source current moment.

We emphasize that in our modeling efforts we did not intend to simulate the quantitatively precise UV photometer response for the two Elves by using a complete modeling of EM wave propagation and excitation of UV emissions in the ionosphere. We rather aimed at qualitatively reproducing the meaningful features of the UV light curves, like shape, rise time, and duration. For more sophisticated and complete modeling efforts of the Elves, see Liu et al. (2017) and Pérez-Invernón et al. (2018).

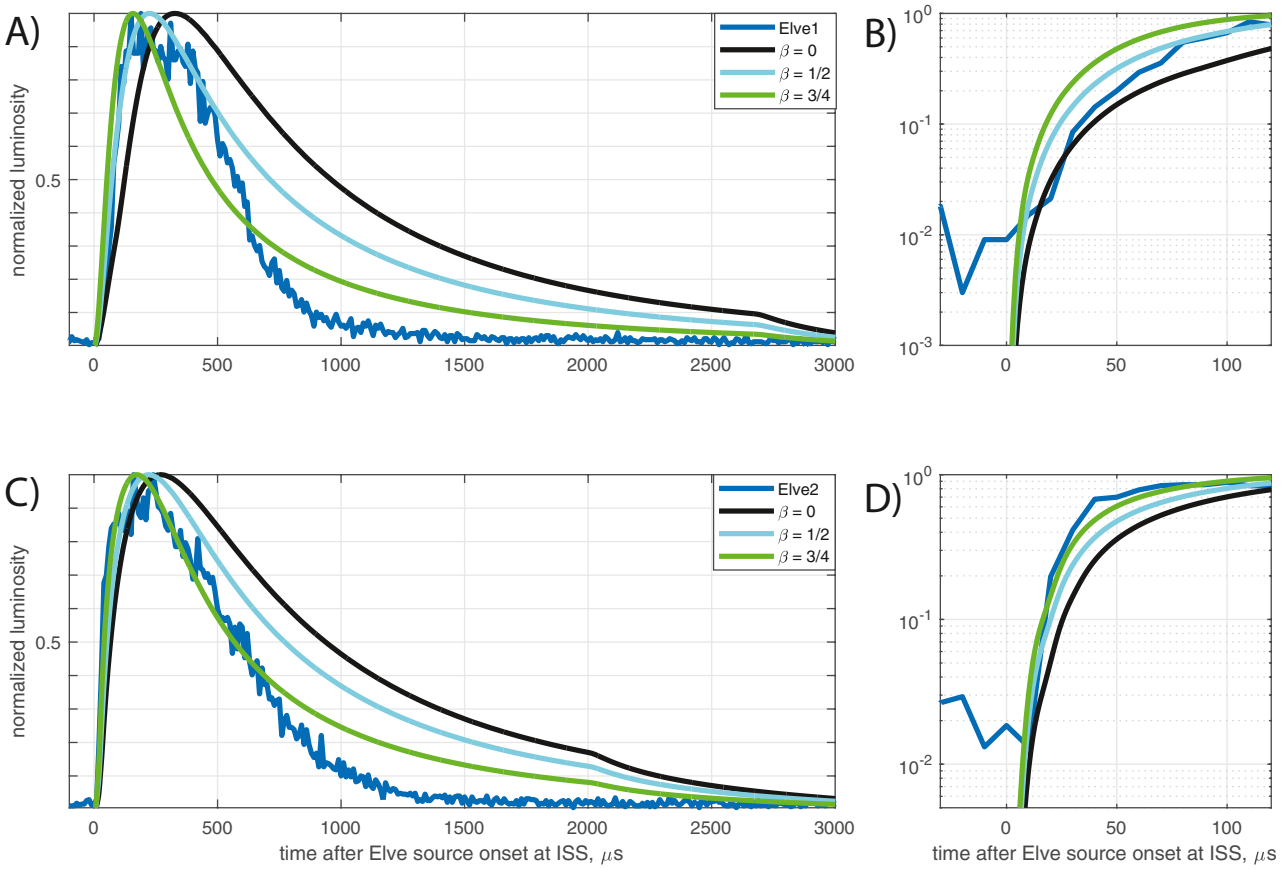

Figure 6. (a) The measured UV signal of the first Elve (blue line) with three modeled signals using the current moment of the EIP as a source and three values of β in Equation 1. (b) Zoomed in version of (a) to show the rising edge of the light curve during initial 100 μs. (c) Same format as (a) for the second Elve. (d) Zoomed in version of (c). The visual onset of both Elves demonstrates a ~10 μs delay compared to the modeled onset. UV, ultra-violet; EIP, energetic in-cloud pulse.

4.3. Scattering of Optical Signals Through the Clouds

To model the scattering and absorption of the 777 nm emissions through the cloud, we follow the procedure described in Luque et al. (2020), their Section 3.1. A point-like lightning source is placed within a homogeneous horizontally infinite cloud bounded by two parallel planes. The source is considered "prompt" and is implemented as a delta function, which is justified by the short duration of the EIP (30 μs, compared to the observed 2 ms long optical pulse) and that the unscattered optical pulse from a RS is typically 40 μs (Jordan et al., 1997). The cloud is composed of water droplets with 10 μm radius and a density of 100 cm^{-3}. These are typical values for clouds and are fixed in our simulations as such, though different values could have been used. As the UV signal is ~10 μs delayed relative to a signal propagating directly to the observational point with the speed of light, the delta function representing the source time plus direct EM propagation time is also fixed to coincide with the onset of the UV signal minus 10 μs for the two events, respectively (green vertical lines in Figure 7). Only two parameters are allowed to vary, the thickness of the cloud and the location of the source relative to the cloud top.

Figure 7 shows the modeling results for the two events, where the pink, blue, and red lines are the measured UV, 337, and 777 nm emissions, respectively. The black line is the modeled 777 nm emissions. For the first event, the combination of a cloud thickness of 12.0 km and a source location of 5.4 km below the cloud top were found to give the best fit with the measurements. Considering a cloud top at 15–16 km, this would give a source at ~10–11 km, which is reasonable production altitude for TGFs (Cummer et al., 2015). Both the delay and rise time and duration of the 777 nm pulse are reproduced fairly well. The long duration is mostly due to scattered light from below the source. For the second event, the best fit with measurements was the

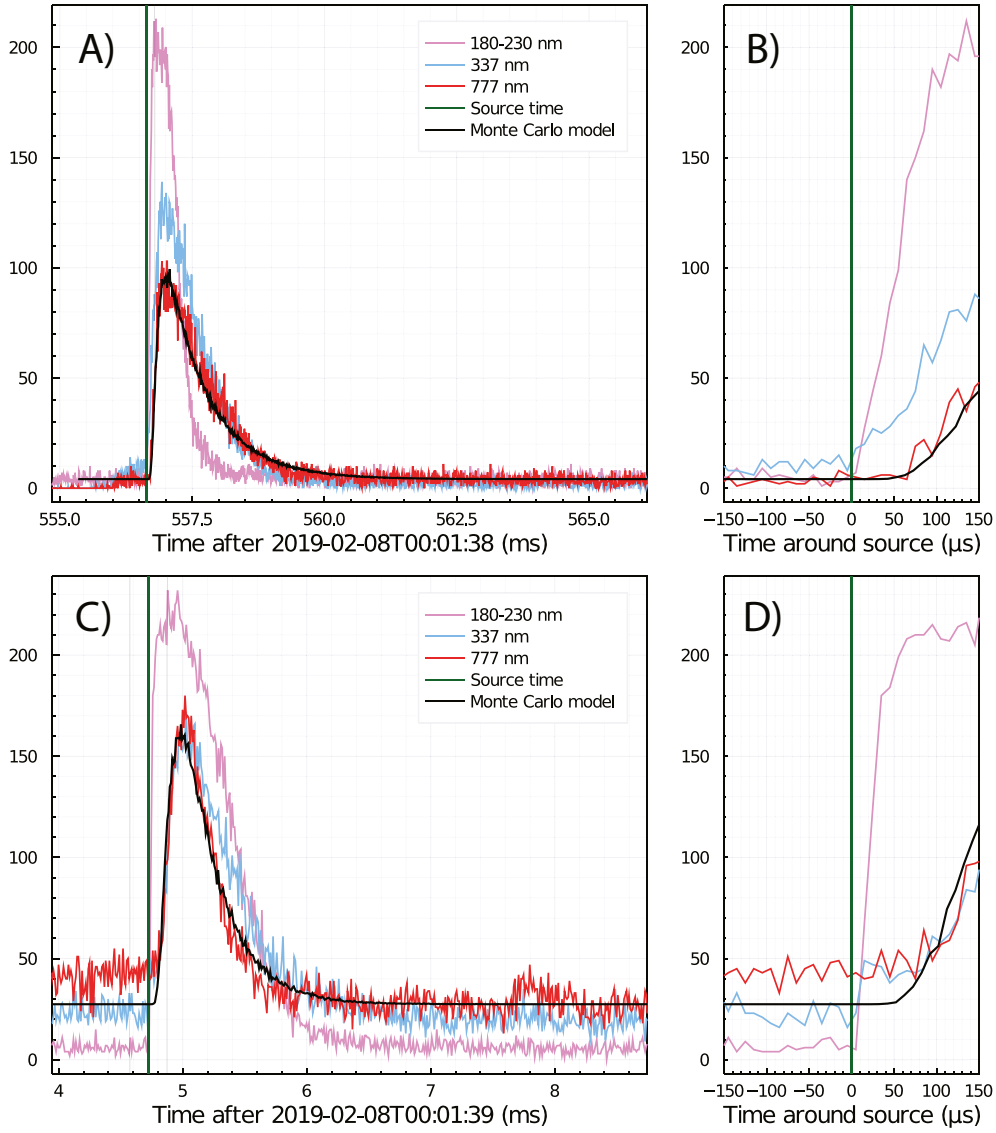

Figure 7. (a) Modeling the 777 nm emissions from the +IC lightning. (b) Zoomed in to see the delayed onset of the 777 nm pulse relative to the source time and UV onset. (c and d) Same as in (a and b), but for the −CG lightning. In all panels: pink, blue, and red lines are the measured UV, 337, and 777 nm emissions, respectively, and source times (UV onset minus 10 µs) are marked with green lines and black lines are the Monte Carlo modeled 777 nm signal. There is 2.5 ms between labels in (a) and 1 ms in (c). For all panels, the measured intensities are in ADC units. IC, intracloud; UV, ultra-violet; CG, cloud-to-ground.

combination of a cloud thickness of only 6.0 km and source location at 5.6 km from cloud top. This would be from the bottom of the cloud. Again, the delay, rise time, and duration are reproduced fairly well, and the short duration is here due to the lack of scattering from below.

Independent modeling of scattering effects on the optical signals detected by ASIM was also performed by one of the coauthors (J. Dwyer) and gave similar rise time and duration (not shown) as the modeling results presented here. We emphasize that there are many free parameters and these results should be considered as some possible ones among others.

5. Discussion

The uniqueness of these observations is that we have both high temporal resolution gamma-ray measurements of a TGF, high-resolution optical signatures in two optical bands of the lightning, the two Elves seen in the UV band and LF radio measurements from both lightning. In addition, we have the locations of the lightning given by WWLLN and GLD360 supported by camera images of the lightning. This combined data set enables us to align the onset of the UV pulse and onset of the LF pulse with a ∼10 μs relative certainty, and then the TGF follows with a ±80 μs relative certainty. We emphasize that the alignment of the data with ∼10 μs relative certainty is only based on the assumption that the EIP and the RS are the sources of the Elves.

The TGF presented here is the second observation (after the first by Neubert et al. [2020]) of a TGF and an Elve produced by the same lightning and gives more support to the prediction by Cummer et al. (2014), Lyu et al. (2015), and Liu et al. (2017) that an EIP associated with a TGF can produce an Elve. It is the first time we also have radio measurements for the analysis, which allows us to identify the EIP and to make a detailed analysis of the event.

For both events, the observed 777 nm emissions are delayed to the observed UV emissions. When modeling the 777 nm emissions we have assumed that the short and large currents (EIP for +IC and RS for −CG, both lasting a few tens of microsecond) produced the large pulse of 777 nm emissions. The optical source was therefore represented by a delta function. Using the UV onset time (minus the 10 μs delay of the UV signal, see Section 4.2) as the time for the optical source inside the cloud, we find that the 777 nm emissions have to propagate a distance of ∼5.5 km between source and cloud top to match the observed delay, shape, and duration of the 777 nm pulses (Figures 7b and 7d). We are not claiming that this is the "true" or the only possible structures of the two clouds, but with reasonable droplet size and density, the model gives reasonable results of both distance from source to cloud top (∼5.5 km) and total cloud thickness (12 and 6 km) and support our assumption of EIP and RS being the source of the 777 nm pulses. The longer duration (2 ms) for the optical signals from the +IC lightning can be explained by scattering in the cloud below the source, while the shorter duration (500 μs) of the optical signal from the −CG lightning is due to the lack of scattering from below, also consistent with the two types of lightning.

Since the EIP and the RS are the only source candidates for the EMP that produced the Elves, we could align the onset of UV signal with the onset of the large pulse in the LF data in both cases, after taking into account the small delay (10 μs) of the UV signals. The EIP and the RS are also the only source candidates in the LF data for the large optical pulses seen in the +IC and the −CG lightning. There are no other candidates.

We also want to point out that with this simple cloud geometry (homogeneous horizontally infinite cloud bounded by two parallel planes) the time delay scales with the square of the distance between source and cloud top. Consequently, distances of 3, 5.5, and 7 km give delays of 25, 80, and 140 μs, respectively, which can serve as reasonable values of expected time delays between the observed optical signal compared to directly propagating signal with the speed of light.

5.1. The +IC Event

We will first consider the +IC event, by discussing the leader propagation and the EIP being the source of both EMP and the large 777 nm pulse, then how TGF is related in time to the EIP and finally what was the current source(s) that produced the short duration and large-amplitude EIP.

5.1.1. Leader Propagation and the EIP During the +IC Event

The LF radio measurements show a few small pulses consistent with leader steps before the large pulse of the +IC, which is accompanied by weak signals in 337 and 777 nm. About 1.1 ms later, a clear signature of a short (30 μs) and intense (280 kA km) EIP is seen in the radio data, and as explained above, this is the only source candidate for both the optical pulse and the EMP that produced the Elve. The EIP has the characteristics needed for making the EMP, it has short duration and large amplitude, and has a steep rise time of only 10 μs and also a short decay time. This is the first large pulse (seen in both radio and optics) in a flash that lasts for about 500 ms (see Figure 2). In the following 1–2 ms, there are spikes seen in the LF

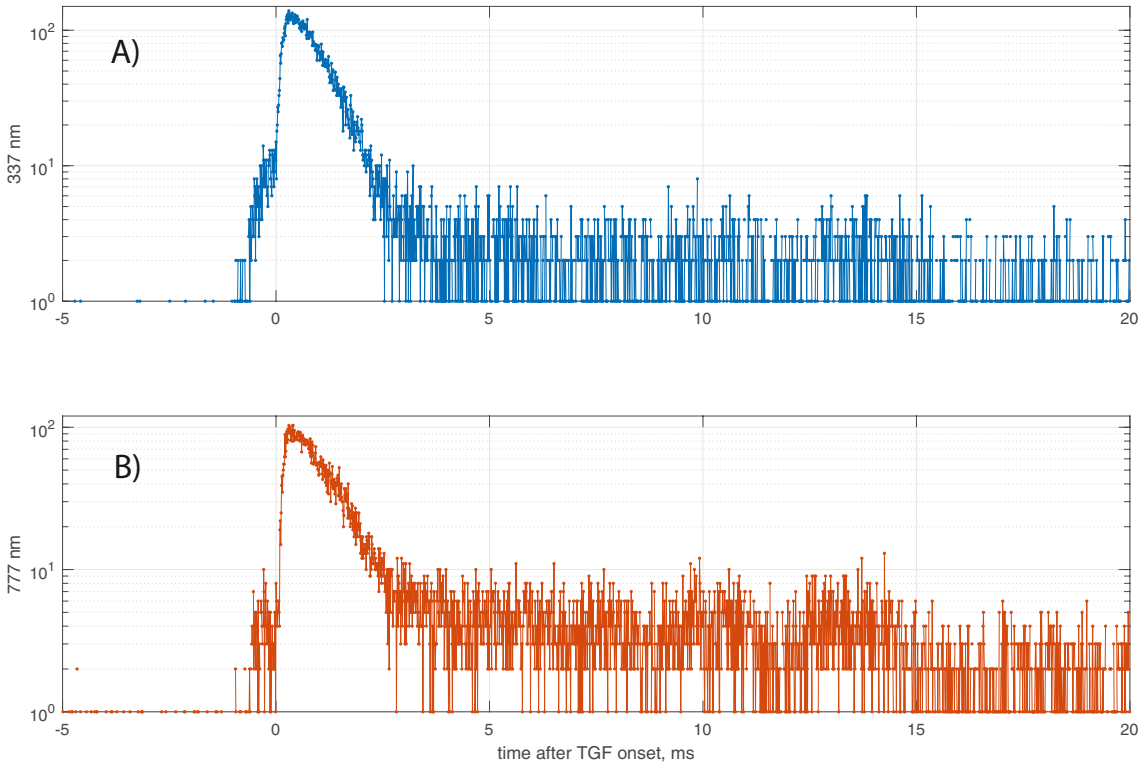

Figure 8. The 337 nm (a) and 777 nm (b) emissions from −5 to 20 ms relative to the TGF onset. The scale is logarithmic to emphasize the weak signals prior to and after the large optical pulse. TGF, terrestrial gamma-ray flash.

data, which could be further leader steps. Also, looking more closely at the 777 nm emissions in the interval from −5 to 20 ms in logarithmic scale, as shown in Figure 8b, we can see that the signal does not decrease to the background level (before the leader started) but stays at the same level as during the leader propagation before the EIP for about 15 ms. This indicates that the leader still propagated either horizontally or vertically after the EIP. In Figures 2e and 2f, frame 2, which covers about 35 ms of this first part of the +IC flash, we see emissions from a very limited area, which suggests vertical propagation, or that the horizontal extension is too faint to be seen when the signal is dominated by the optical pulse from the EIP. We can therefore not conclude that the EIP (and the TGF as will be discussed below) was produced at the end of the vertical leader propagation, but rather that there was still vertical propagation after the EIP and TGF, consistent with earlier reports (Cummer et al., 2015; Lu et al., 2010; Shao et al., 2010; Stanley et al., 2006), but contrary to the EIP recently reported by Tilles et al. (2020), who reported no further leader propagation after that EIP, and for this reason they termed it an "unusual" EIP. Since the optical signals of this propagation were rather weak, it could be that this was when the leader propagated into the positive charge region where the relative potential (between leader and ambient) becomes smaller and smaller with further vertical propagation. The continuous leader propagation is also seen in the 337 nm emissions (Figure 8a), but we also notice that the 337 nm preactivity is more intense than in the 777 nm, which could indicate that in addition to the leader, also streamers contributed significantly to the 337 nm emissions in the pre-EIP leader propagation. About 100 ms later, there are many large optical pulses (Figure 2c) and the camera images (frames 3 and 4) indicate activity over an extended horizontal area.

5.1.2. The Time Sequence of the TGF and the EIP

As the relative timing between the MMIA and MXGS is not better than ±80 μs, we do not know the exact timing of the onset of the TGF relative to the EIP. We can only state with confidence that the TGF was produced either just before (<60 μs), simultaneous, or just after (<100 μs) the EIP. However, it should be noticed that for the event reported by Neubert et al. (2020), we had ±5 μs relative timing accuracy, and the onset of the TGF preceded the onset of UV signal by 20 μs ± 5 μs and that the short TGF was almost

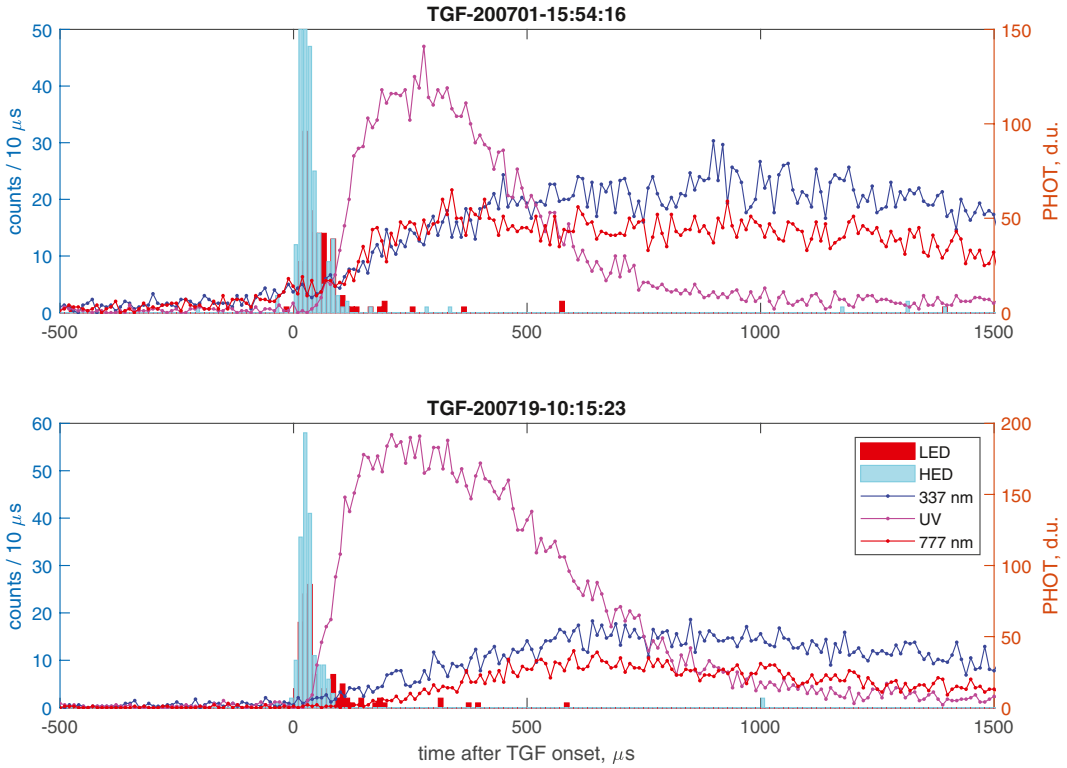

Figure 9. Two examples of TGF and Elves, where the timing uncertainty between MXGS and MMIA is ±5 μs. TGF, terrestrial gamma-ray flash; MXGS, modular X- and gamma-ray sensor; and MMIA, modular multispectral imaging array.

terminated when the UV signal increased, as seen in their Figure 2b. By August 2020, we have six more observations of TGFs that occurred simultaneously with Elves. In all of these, the onset of the TGF is before or simultaneous with the onset of the UV signal of the Elve with a relative timing accuracy between MMIA and MXGS of ±5 μs. For these six events, GLD360 reported peak currents range from 280 to 400 kA. In Figure 9, we show two of these events, where the TGF onset is ~30–40 μs before the UV onset. These will be subject to further studies, but here we just want to point out the consistent time sequence between TGFs and Elves. We therefore think it is most likely that also the TGF reported here was either before or simultaneous with the EIP and not after. In Figure 10, we show how the shape of the TGF seen in the HED (blue) follows the current moment pulse derived from the LF measurements, when moved 30 μs earlier, which is well within the ±80 μs uncertainty.

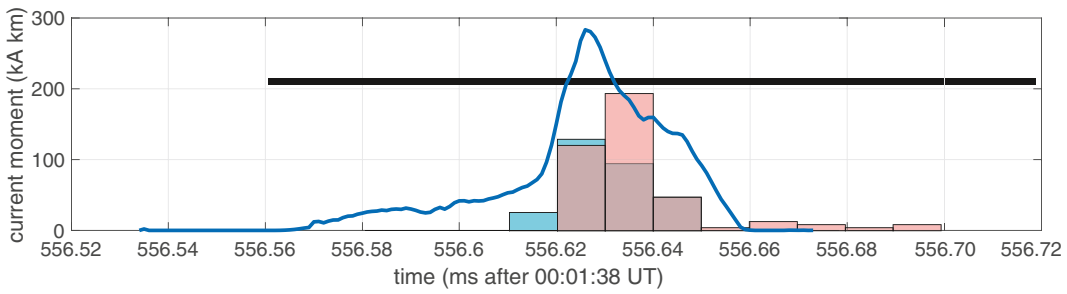

Figure 10. The current moment derived from LF measurements and the TGF, when moved 30 μs earlier. The black bar is the uncertainty of ±80 μs of the TGF time centered at 556.64 ms. Blue bars are HED, while red bars are LED. LF, low frequency; TGF, terrestrial gamma-ray flash; HED, high energy detector; LED, low-energy detector.

5.1.3. Possible Current Sources for the EIP

We can think of two types of current that could produce the EIP: (1) a current in a hot leader channel and (2) the current from the TGF itself. We will discuss both candidates and the combination of the two.

5.1.3.1. A Current in a Hot Channel

Since 777 nm emissions are produced through dissociative excitation of molecular oxygen it is considered to be produced in the hot channel of a leader (Chanrion et al., 2019). It should be noticed that the 777 nm pulse is a fairly intense pulse of 100 ADC above the preactivity level. The short duration of the TGF indicates that the strong electric field that accelerated the electrons in the Relativistic Runaway Electron Avalanche (RREA) process (Gurevich et al., 1992) (and maybe feedback [Dwyer, 2012]) also had a short duration and could have been quenched when the leader made a connection with another conductive body to produce a large radio pulse. This would imply that the TGF was not directly related to the EIP, but that they are two phenomena that occurred simultaneously. For a TGF, we need large potential drop and an electric field above the RREA threshold, which could be facilitated by a long leader. The strong current that produced the EIP could occur when this long leader connected to some conductive body (e.g., another leader channel/stem) and a current would flow through the hot leader channel.

In Østgaard, Neubert, et al. (2019), it was speculated whether this connection is made at the lower end or upper end of the leader. If the connection is made at the lower end, and assuming that we only see the optical signatures when the current wave through the leader has reached the top of the leader, the delay between the onset of the current pulse and the onset of the optical pulse could be as much as ∼70 μs (assuming a 4 km long leader and wave speed of $\frac{1}{5}$ of speed of light [Liang et al., 2014]), in addition to the delay caused by scattering in the cloud. If this is the case we should have seen a larger delay between the UV signal (which we aligned with the LF) and the 777 nm than the ∼70 μs we observed. However, if the speed of the current wave is at the upper limit ($\frac{1}{3}$ of speed of light [Liang et al., 2014]) the propagation time would be less than 20 μs and with our time resolution we cannot resolve this. If the connection is at the lower end, it is not obvious that the electric field ahead of the upper part of the leader should be quenched, which the short duration of the TGF indicates. A connection at the upper part of the leader would indeed terminate the electric field ahead of the leader, but positive leaders coming down from the positive charge region have not been observed. So, at this point, this is just speculation.

Due to this scenario, the TGF should be produced just before the EIP. To be consistent with the results by Cummer et al. (2011, 2015) and Pu et al. (2019) who all showed that the pulses from EIPs and the TGFs were correlated down to <10 μs, the TGF could not precede the EIP by much.

5.1.3.2. The Current From the TGF Itself

As modeling results (Dwyer & Cummer, 2013) and measurements (Connaughton et al., 2013; Cummer et al., 2011, 2015; Mezentsev et al., 2017; Pu et al., 2019) have suggested that a TGF also represents a current that would give radio emissions, we will consider a scenario, where the EIP was *not* a current in the hot channel but from the TGF itself, which is ahead (outside) the leader tip. In this case, it is the electrons in the RREA process and their secondaries that make the current that produces the EIP. This was also interpreted to be the source of the EIP in a recent paper by Tilles et al. (2020). In this scenario also, the feedback process could have been involved. It should be noticed that in this short TGF the count rate was so high that the HED instrument missed counts during the peak intensity, so the TGF current could have been large.

We also notice that the EIP and TGF had the same duration of 30 μs. Typical duration of EIPs observed simultaneous with TGFs on microsecond time scale has been reported to be from 30 μs (Cummer et al., 2011, 2015) to 80 μs (Pu et al., 2019). In this scenario, the termination of the electric field that produced the TGF could have been facilitated by the feedback process, which can easily decrease the electric field in tens of microseconds.

This scenario would be consistent with the TGFs that were observed to be simultaneous with the optical pulses in Østgaard, Neubert, et al. (2019), but not with the $\frac{1}{3}$ of the TGFs that preceded the optical pulse by

more than 180 μs (uncertainty of 80 μs plus a delay of 100 μs). There has been modeling efforts to estimate the optical emissions associated with TGFs (Xu et al., 2015) but they did not include 777 nm emissions, and we are not aware of any studies that have done that. Since the current from the TGF itself would not be in a hot channel, it is not obvious how this current could produce such strong pulse of 777 nm emissions, which requires high temperature. We also want to point out that there is a weaker current moment (~60 kA km) prior to the EIP lasting for at least 50 μs (see Figure 5b). We cannot exclude the possibility that this could be the signature of the TGF current. This interpretation would be consistent with the EIP being produced by a current flowing in a hot channel, but again inconsistent with results showing that EIPs and TGFs are correlated down to <10 μs (Cummer et al., 2011, 2015; Pu et al., 2019).

A current in a hot channel is the most likely candidate for producing the large 777 nm pulse. On the other hand, the duration of the TGF is exactly the same duration as the derived current moment changes from the LF measurements. This suggests that the EIP could be produced by a combination of the two, that there was a current in a hot channel and that the TGF current was simultaneous and contributed significantly to the total current observed as an EIP. In this case, the 777 nm emissions were produced by the hot-channel current, consistent with the high temperature required for the dissociative excitation of molecular oxygen to produce the emissions.

For both scenarios, a large electric field ahead of a long leader seems to be a prerequisite. As the leader extends vertically toward the "center" positive charge region, the potential difference between leader tip and ambient increases while the RREA electric field threshold, which scales with the neutral density, decreases with altitude. This means that there is an altitude range that is favorable for producing a TGF. In addition, the total electric field (the leader field and ambient field) needs to stay above the RREA threshold for a sufficient long distance to provide the potential difference needed for RREA (and feedback) to occur (Celestin et al., 2015; Dwyer, 2012; Skeltved et al., 2014). As the ambient field gets smaller inside the positive charge region (and changes polarity in the "center"), its contribution to the total electric field gets smaller and the potential difference between the leader tip and ambient may not be sufficient for producing a TGF. This implies that the relative position (in altitude) of leader tip and positive charge "center" also might be important for producing a TGF. In the case where the conditions for producing TGF *are* satisfied, the leader can still propagate vertically in the positive charge region (as discussed earlier) and this can explain why the TGF is not produced when the leader is even longer, a question raised by Cummer et al. (2015).

5.2. The −CG Event

The second Elve was produced by an EMP from the RS of a −CG. According to both the GLD360/WWLLN and camera images, the −CG occurred about 300 km south of the +IC lightning. The optical pulse of the −CG lightning is on top of the light from the IC flash (Figures 2b, 2e, and 2f, frame 7). Before the RS, there are continuous activity in the LF data, as expected for a −CG lightning. The large LF pulse of the RS was the first RS in a flash that has several LF pulses from the same region 300, 700, and 800 ms after the RS (not shown). No activity was seen in MMIA camera images or by GLD360 and WWLLN from this cloud before the preactivity and RS. This Elve is similar to the early observations of Elves that were related to CG lightning of both polarities (e.g., Fukunishi et al., 1996; Inan et al., 1997). Since the RS represents a large current flowing in a hot channel, it would also be the only candidate for producing the large optical pulses. Our modeling of the 777 nm emissions through the cloud also reproduces the delay between UV pulse and 777 nm pulse, as well as its shape and duration. For this study, the importance of having the second Elve observation 456 ms after the first one is that it enabled a time alignment of the LF data and MMIA data with 10 μs accuracy, which was essential for the detailed analysis of the EIP, the optical pulses, and the TGF.

6. Conclusions

Based on both radio, optical, and gamma-ray data, and modeling of light scattering in a cloud and Elve production, we can conclude the following:

(1) The sources of the EM pulses that produced the two Elves were the EIP in the +IC lightning and the RS in the −CG lightning.
(2) The EIP and the RS were also the sources for the large pulses seen in 777 nm emissions.
(3) The first Elve and the TGF were produced during the vertical leader propagation in the initial phase of the +IC.
(4) The TGF is produced before or most likely simultaneously with source of the EIP.

The EIP was produced by a current in a hot channel, the current from the TGF itself, or a combination of the two. The duration of the EIP is consistent with both current sources, while the strong 777 nm pulse favors a current in a hot channel. Since the TGF is both short and intense and should produce a strong current, it is likely that the EIP is produced by a combination of the two current sources occurring simultaneously. The termination of the electric field that produced the TGF could have been that the leader connected to another conductive body, or it was the TGF itself that reduced the field.

Appendix A: A.1. Leader Activity Prior to the Large Optical Pulse of the +IC Lightning

Figure A1 is a zoomed in version of Figures 3a, 3c, and 3e in logarithmic scale to show the weak signals in LF that start at 555.5 ms and continue around 556 ms, and how the optical signals in 337 and 777 nm start increasing soon after 555.5 ms.

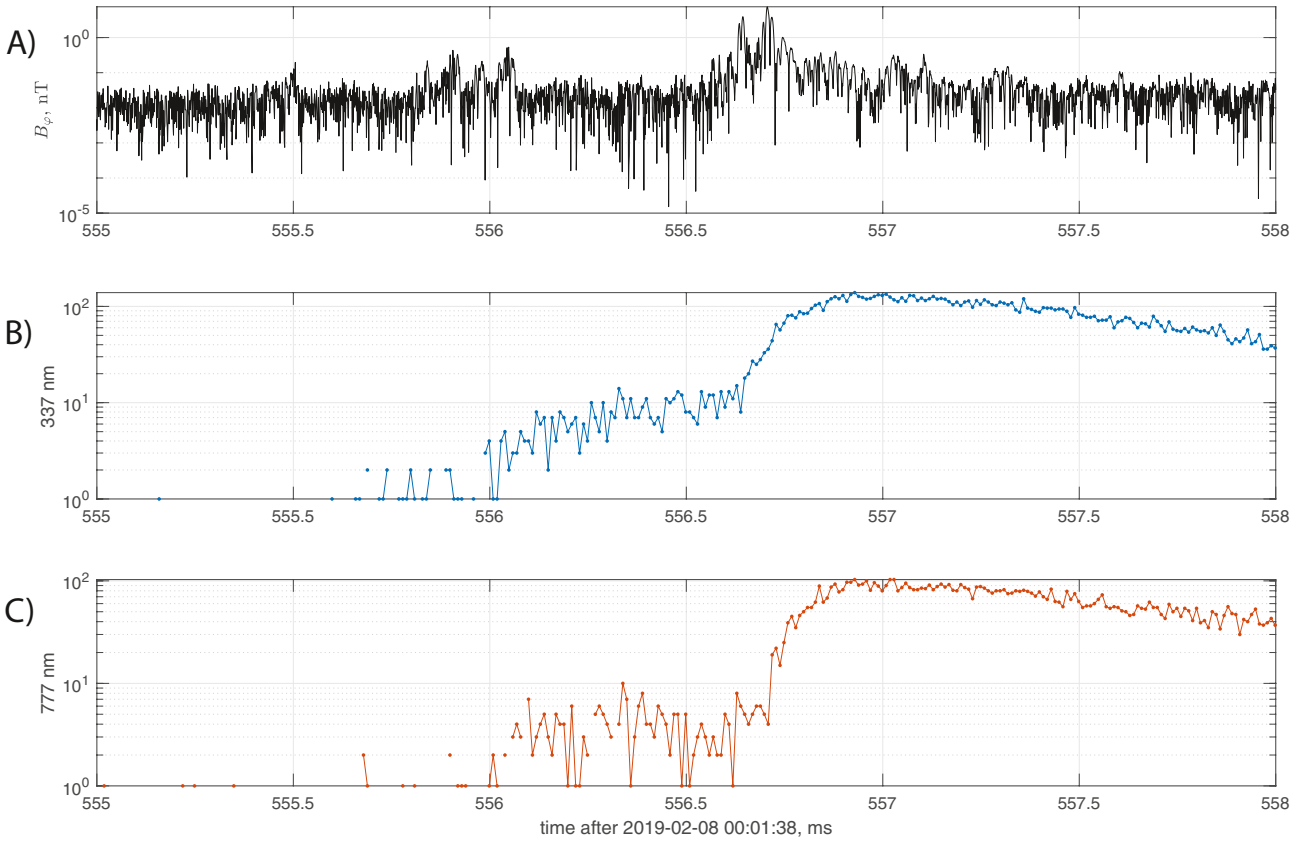

Figure A1. The leader preactivity prior to the EIP, TGF, and Elve. (a) LF from Puerto Rico. (b) MMIA PHOT 337 nm. (c) MMIA PHOT 777 nm in logarithmic scale. For panels (b and c), the intensities are in ADC units. EIP, energetic in-cloud pulse; TGF, terrestrial gamma-ray flash; LF, low frequency; MMIA, modular multispectral imaging array.

A.2. Leader Activity Prior to the Large Optical Pulse of the −CG Lightning

Figure A2 shows an extended time interval of Figure 4a in logarithmic scale. From about 2.5 ms, there is an increase in the LF signals, which indicate the continuous activity of a downward negative leader for about 2 ms before the large RS pulse of the −CG.

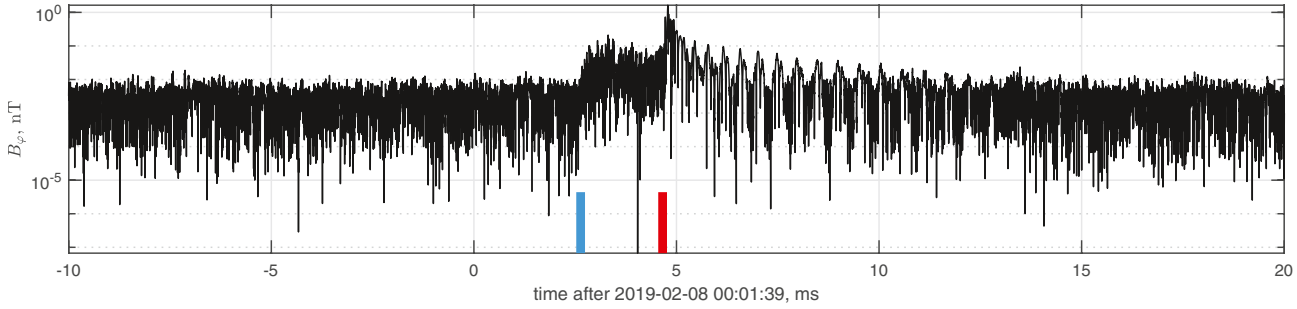

Figure A2. The preactivity (starting at ∼2.6 ms, blue bar) seen in LF from Puerto Rico prior to the RS (at ∼4.7 ms, red bar) of the −CG lightning. LF, low frequency; RS, return stroke; CG, cloud-to-ground.

Data Availability Statement

The data described in this study are available from the authors on request (nikolai.ostgaard@uib.no) and can also be downloaded from the Asim Science Data Centre (ASDC) homepage after a proposal has been submitted and approved. All the data that are used to produce the figures in this paper are uploaded to Zenodo: https://doi.org/10.5281/zenodo.4316610.

Acknowledgments
This study was supported by the European Research Council under the European Union's Seventh Framework Programme (FP7/2007–2013)/ERC grant agreement no. 320839 and the Research Council of Norway under contracts 223252/F50 (CoE). This study has received funding from the European Union's Horizon 2020 research and innovation program under the Marie Skłodowska-Curie grant agreement SAINT 722337. A.L. acknowledges support by the European Research Council (ERC) under the European Union H2020 program/ERC grant agreement 681257. This work was supported by the National Science Foundation Dynamic and Physical Meteorology program through grant AGS/1565606. The authors thank the International Space Science Institute, Bern, Switzerland, for providing financial support and meeting facilities in the frame of the International Team no. 471: Understanding the Properties of the Terrestrial Gamma-Ray Flash Population.

References

Bogomolov, V. V., Panasyuk, M. I., Svertilov, S. I., Bogomolov, A. V., Garipov, G. K., Iyudin, A. F., et al. (2017). Observation of terrestrial gamma-ray flashes in the RELEC space experiment on the Vernov satellite. *Cosmic Research*, *55*(3), 159–168. https://doi.org/10.1134/S0010952517030017

Briggs, M. S., Fishman, G. J., Connaughton, V., Bhat, P. N., Paciesas, W. S., Preece, R. D., et al. (2010). First results on terrestrial gamma ray flashes from the Fermi Gamma-ray Burst Monitor. *Journal of Geophysical Research*, *115*, A07323. https://doi.org/10.1029/2009JA015242

Celestin, S., Xu, W., & Pasko, V. P. (2015). Variability in fluence and spectrum of high-energy photon bursts produced by lightning leaders. *Journal of Geophysical Research: Space Physics*, *120*, 10712–10723. https://doi.org/10.1002/2015JA021410

Chanrion, O., Neubert, T., Lundgaard Rasmussen, I., Stoltze, C., Tcherniak, D., Jessen, N. C., et al. (2019). The modular multispectral imaging array (MMIA) of the ASIM payload on the International Space Station. *Space Science Reviews*, *215*(4), 28. https://doi.org/10.1007/s11214-019-0593-y

Connaughton, V., Briggs, M. S., Xiong, S., Dwyer, J. R., Hutchins, M. L., Grove, J. E., et al. (2013). Radio signals from electron beams in terrestrial gamma ray flashes. *Journal of Geophysical Research: Space Physics*, *118*, 2313–2320. https://doi.org/10.1029/2012JA018288

Cummer, S. A., Briggs, M. S., Dwyer, J. R., Xiong, S., Connaughton, V., Fishman, G. J., et al. (2014). The source altitude, electric current, and intrinsic brightness of terrestrial gamma ray flashes. *Geophysical Research Letters*, *41*, 8586–8593. https://doi.org/10.1002/2014GL062196

Cummer, S. A., & Inan, U. S. (2000). Modeling ELF radio atmospheric propagation and extracting lightning currents from elf observations. *Radio Science*, *35*(2), 385–394. https://doi.org/10.1029/1999RS002184

Cummer, S. A., Lu, G., Briggs, M. S., Connaughton, V., Xiong, S., Fishman, G. J., & Dwyer, J. R. (2011). The lightning–TGF relationship on microsecond timescales. *Geophysical Research Letters*, *38*, L14810. https://doi.org/10.1029/2011GL048099

Cummer, S. A., Lyu, F., Briggs, M. S., Fitzpatrick, G., Roberts, O. J., & Dwyer, J. R. (2015). Lightning leader altitude progression in terrestrial gamma-ray flashes. *Geophysical Research Letters*, *42*, 7792–7798. https://doi.org/10.1002/2015GL065228

Cummer, S. A., Zhai, Y., Hu, W., Smith, D. M., Lopez, L. I., & Stanley, M. A. (2005). Measurements and implications of the relationship between lightning and terrestrial gamma ray flashes. *Geophysical Research Letters*, *32*, L08811. https://doi.org/10.1029/2005GL022778

Dwyer, J. R. (2012). The relativistic feedback discharge model of terrestrial gamma ray flashes. *Journal of Geophysical Research*, *117*, A02308. https://doi.org/10.1029/2011JA017160

Dwyer, J. R., & Cummer, S. A. (2013). Radio emissions from terrestrial gamma-ray flashes. *Journal of Geophysical Research: Space Physics*, *118*, 3769–3790. https://doi.org/10.1002/jgra.50188

Dwyer, J. R., & Smith, D. M. (2005). A comparison between Monte Carlo simulations of runaway breakdown and terrestrial gamma-ray flash observations. *Geophysical Research Letters*, *32*, L22804. https://doi.org/10.1029/2005GL023848

Fishman, G. J., Bhat, P. N., Mallozzi, R., Horack, J. M., Koshut, T., Kouveliotou, C., et al. (1994). Discovery of intense gamma-ray flashes of atmospheric origin. *Science*, *264*, 1313–1316.

Fukunishi, H., Takahashi, Y., Kubota, M., Sakanoi, K., Inan, U. S., & Lyons, W. A. (1996). Elves: Lightning-induced transient luminous events in the lower ionosphere. *Geophysical Research Letters*, *23*(16), 2157–2160. https://doi.org/10.1029/96GL01979

Gjesteland, T., Østgaard, N., Bitzer, P., & Christian, H. J. (2017). On the timing between terrestrial gamma ray flashes, radio atmospherics, and optical lightning emission. *Journal of Geophysical Research: Space Physics*, *122*, 7734–7741. https://doi.org/10.1002/2017JA024285

Gurevich, A. V., Milikh, G. M., & Roussel-Dupré, R. (1992). Runaway electron mechanism of air breakdown and preconditioning during a thunderstorm. *Physics Letters A*, *165*(5–6), 463–468. https://doi.org/10.1016/0375-9601(92)90348-P

Hutchins, M. L., Holzworth, R. H., Brundell, J. B., & Rodger, C. J. (2012). Relative detection efficiency of the World Wide Lightning Location Network. *Radio Science*, *47*, RS6005. https://doi.org/10.1029/2012RS005049

Inan, U. S., Barrington-Leigh, C., Hansen, S., Glukhov, V. S., Bell, T. F., & Rairden, R. (1997). Rapid lateral expansion of optical luminosity in lightning-induced ionospheric flashes referred to as 'elves'. *Geophysical Research Letters*, *24*(5), 583–586. https://doi.org/10.1029/97GL00404

ITU. (2007). Ground-wave propagation curves for frequencies between 10 kHz and 30 MHz. *Recommendation International Telecommunication Union* (02), 368–369.

Jordan, D. M., Rakov, V. A., Beasley, W. H., & Uman, M. A. (1997). Luminosity characteristics of dart leaders and return strokes in natural lightning. *Journal of Geophysical Research*, *102*(D18), 22025–22032.

Liang, C., Carlson, B., Lehtinen, N., Cohen, M., Marshall, R. A., & Inan, U. (2014). Differing current and optical return stroke speeds in lightning. *Geophysical Research Letters*, *41*, 2561–2567. https://doi.org/10.1002/2014GL059703

Liu, N., Dwyer, J. R., & Cummer, S. A. (2017). Elves accompanying terrestrial gamma ray flashes. *Journal of Geophysical Research: Space Physics*, *122*, 10563–10576. https://doi.org/10.1002/2017JA024344

Lu, G., Blakeslee, R. J., Li, J., Smith, D. M., Shao, X.-M., McCaul, E. W., et al. (2010). Lightning mapping observation of a terrestrial gamma-ray flash. *Geophysical Research Letters*, *37*, L11806. https://doi.org/10.1029/2010GL043494

Luque, A., Gordillo-Vázquez, F. J., Li, D., Malagón-Romero, A., Pérez-Invernón, F. J., Schmalzried, A., et al. (2020). Modeling lightning observations from space-based platforms (CloudScat.jl 1.0). *Geoscientific Model Development*, *13*, 5549–5566. https://doi.org/10.5194/gmd-13-5549-2020

Lyu, F., Cummer, S. A., & McTague, L. (2015). Insights into high peak current in-cloud lightning events during thunderstorms. *Geophysical Research Letters*, *42*, 6836–6843. https://doi.org/10.1002/2015GL065047

Marisaldi, M., Fuschino, F., Labanti, C., Galli, M., Longo, F., Monte, E. D., et al. (2010). Detection of terrestrial gamma ray flashes up to 40 MeV by the AGILE satellite. *Journal of Geophysical Research*, *107*, A00E13. https://doi.org/10.1029/2009JA014502

Marshall, R. A., da Silva, C. L., & Pasko, V. P. (2015). Elve doublets and compact intracloud discharges. *Geophysical Research Letters*, *42*, 6112–6119. https://doi.org/10.1002/2015GL064862

Mezentsev, A., Lehtinen, N., Østgaard, N., Pérez-Invernón, F. J., & Cummer, S. A. (2018). Spectral characteristics of VLF Sferics associated with RHESSI TGFs. *Journal of Geophysical Research: Atmospheres*, *123*, 139–159. https://doi.org/10.1002/2017JD027624

Neubert, T., Østgaard, N., Reglero, V., Blanc, E., Chanrion, O., Oxborrow, C. A., et al. (2019). The ASIM mission on the International Space Station. *Space Science Reviews*, *215*(2), 26. https://doi.org/10.1007/s11214-019-0592-z

Neubert, T., Østgaard, N., Reglero, V., Chanrion, O., Heumesser, M., Dimitriadou, K., et al. (2020). A terrestrial gamma-ray flash and ionospheric ultraviolet emissions powered by lightning. *Science*, *367*(6474), 183–186. https://doi.org/10.1126/science.aax3872

Østgaard, N., Balling, J. E., Bjørnsen, T., Brauer, P., Budtz-Jørgensen, C., Bujwan, W., et al. (2019). The modular X- and gamma-ray sensor (MXGS) of the ASIM Payload on the International Space Station. *Space Science Reviews*, *215*(2), 23. https://doi.org/10.1007/s11214-018-0573-7

Østgaard, N., Gjesteland, T., Carlson, B. E., Collier, A. B., Cummer, S. A., Lu, G., & Christian, H. J. (2013). Simultaneous observations of optical lightning and terrestrial gamma ray flash from space. *Geophysical Research Letters*, *40*, 2423–2426. https://doi.org/10.1002/grl.50466

Østgaard, N., Neubert, T., Reglero, V., Ullaland, K., Yang, S., Genov, G., et al. (2019). First 10 months of TGF observations by ASIM. *Journal of Geophysical Research: Atmospheres*, *124*, 14024–14036. https://doi.org/10.1029/2019JD031214

Pérez-Invernón, F. J., Luque, A., Gordillo-Vázquez, F. J., Sato, M., Ushio, T., Adachi, T., & Chen, A. B. (2018). Spectroscopic diagnostic of halos and Elves detected from space-based photometers. *Journal of Geophysical Research: Atmospheres*, *128*, 12917–12941. https://doi.org/10.1029/2018JD029053

Pu, Y., Cummer, S. A., Lyu, F., Briggs, M., Mailyan, B., Stanbro, M., & Roberts, O. (2019). Low frequency radio pulses produced by terrestrial gamma-ray flashes. *Geophysical Research Letters*, *46*, 6990–6997. https://doi.org/10.1029/2019GL082743

Rodger, C. J., Brundell, J. B., & Dowden, R. L. (2005). Location accuracy of VLF World-Wide Lightning Location (WWLL) network: Post-algorithm upgrade. *Annales Geophysicae*, *23*, 277–290. https://doi.org/10.5194/angeo-23-277-2005

Rudlosky, S. D., Peterson, M. J., & Kahn, D. T. (2017). GLD360 performance relative to TRMM LIS. *Journal of Atmospheric and Oceanic Technology*, *34*, 1307–1322. https://doi.org/10.1175/JTECH-D-16-0243.1

Said, R. K., Inan, U. S., & Cummins, K. L. (2010). Long-range lightning geolocation using a VLF radio atmospheric waveform bank. *Journal of Geophysical Research*, *115*, D23108. https://doi.org/10.1029/2010JD013863

Schmit, T. J., Griffith, P., Gunshor, M. M., Daniels, J. M., Goodman, S. J., & Lebair, W. J. (2017). A closer look at the ABI on the GOES-R series. *Bulletin of the American Meteorological Society*, *98*(4), 681–698. https://doi.org/10.1175/BAMS-D-15-00230.1

Shao, X.-M., Hamlin, T., & Smith, D. M. (2010). A closer examination of terrestrial gamma-ray flash-related lightning processes. *Journal of Geophysical Research*, *115*, A00E30. https://doi.org/10.1029/2009JA014835

Shao, X.-M., Jacobsen, A. R., & Fitzgerald, T. J. (2004). Radio frequency radiation beam pattern of lightning return strokes: A revisit to theoretical analysis. *Journal of Geophysical Research*, *109*, D19108. https://doi.org/10.1029/2004JD004612

Šimek, M. (2014). Optical diagnostics of streamer discharges in atmospheric gases. *Journal of Physics D Applied Physics*, *47*, 463001. https://doi.org/10.1088/0022-3727/47/46/463001

Skeltved, A. B., Østgaard, N., Carlson, B., Gjesteland, T., & Celestin, S. (2014). Modeling the Relativistic Runaway Electron Avalanche and the feedback mechanism with GEANT4. *Journal of Geophysical Research: Space Physics*, *119*, 9174–9191. https://doi.org/10.1002/2014JA020504

Smith, D. M., Lopez, L. L., Lin, R. P., & Barrington-Leigh, C. P. (2005). Terrestrial gamma-ray flashes observed up to 20 MeV. *Science*, *307*, 1085–1088.

Stanley, M. A., Shao, X.-M., Smith, D. M., Lopez, L. I., Pongratz, M. B., Harlin, J. D., et al. (2006). A link between terrestrial gamma-ray flashes and intracloud lightning discharges. *Geophysical Research Letters*, *33*, L06803. https://doi.org/10.1029/2005GL025537

Tilles, J. N., Krehbiel, P. R., Stanley, M. A., Rison, W., Liu, N., Lyu, F., et al. (2020). Radio interferometer observations of an energetic in-cloud pulse reveal large currents generated by relativistic discharges. *Journal of Geophysical Research: Atmospheres*, *125*, e2020JD032,603. https://doi.org/10.1029/2020JD032603

Uman, M. A., McLain, D. K., & Krider, E. P. (1975). The electromagnetic radiation from a finite antenna. *American Journal of Physics*, *43*(43), 33–38. https://doi.org/10.1119/1.10027

Ursi, A., Guidorzi, C., Marisaldi, M., Sarria, D., & Frontera, F. (2017). Terrestrial gamma-ray flashes in the BeppoSAX data archive. *Journal of Atmospheric and Solar-Terrestrial Physics*, *156*, 50–56. https://doi.org/10.1016/j.jastp.2017.02.014

Xu, W., Celestin, S., & Pasko, V. P. (2015). Optical emissions associated with terrestrial gamma ray flashes. *Journal of Geophysical Research: Space Physics*, *120*, 1355–1370. https://doi.org/10.1002/2014JA020425